Charge Carrier Induced Structural Ordering And Disordering in Organic Mixed Ionic Electronic Conductors

Tyler J. Quill, Garrett LeCroy, Adam Marks, Sarah A. Hesse, Quentin Thiburce, Iain McCulloch, Christopher J. Tassone, Christopher J. Takacs, Alexander Giovannitti, and Alberto Salleo**

Operational stability underpins the successful application of organic mixed ionic-electronic conductors (OMIECs) in a wide range of fields, including biosensing, neuromorphic computing, and wearable electronics. In this work, both the operation and stability of a p-type OMIEC material of various molecular weights are investigated. Electrochemical transistor measurements reveal that device operation is very stable for at least 300 charging/discharging cycles independent of molecular weight, provided the charge density is kept below the threshold where strong charge–charge interactions become likely. When electrochemically charged to higher charge densities, an increase in device hysteresis and a decrease in conductivity due to a drop in the hole mobility arising from long-range microstructural disruptions are observed. By employing *operando* X-ray scattering techniques, two regimes of polaron-induced structural changes are found: 1) polaron-induced structural ordering at low carrier densities, and 2) irreversible structural disordering that disrupts charge transport at high carrier densities, where charge–charge interactions are significant. These *operando* measurements also reveal that the transfer curve hysteresis at high carrier densities is accompanied by an analogous structural hysteresis, providing a microstructural basis for such instabilities. This work provides a mechanistic understanding of the structural dynamics and material instabilities of OMIEC materials during device operation.

1. Introduction

Organic mixed ionic-electronic conductors (OMIECs) are organic semiconductors capable of transporting both ionic and electronic charges. The dual-conducting nature of OMIEC materials enables ionic signals to be transduced into electronic currents through the process of volumetric doping, where changes in ion concentration in the bulk of the material modulate the electronic conductivity of the semiconductor. The combination of this transduction and volumetric doping makes OMIECs attractive in a wide range of fields including energy storage, neuromorphic computing, and bioelectronics.[1] The prototypical OMIEC device is the organic electrochemical transistor (OECT), which leverages the volumetric doping of OMIEC materials to efficiently transduce small ionic currents into large changes in electronic conductivity, enabling the real-time readout of biological signals.[2] The high transconductance of OMIEC materials arises because of the large number of highly mobile charges which can be stabilized on the polymer backbone. The electronic carrier mobility, μ, and the volumetric capacitance, C^*, along with the threshold voltage, are the materials properties responsible for this high transconductance. Recently, a multitude of synthetic efforts have aimed to enhance the performance of OMIEC materials by increasing these values. These efforts have ranged from increasing backbone planarity (to extend charge delocalization and improve charge transport)[3–5] to engineering side chain chemistry (to facilitate ionic penetration thus increasing C^* while enabling processability).[6,7]

T. J. Quill, G. LeCroy, A. Marks, Q. Thiburce, A. Giovannitti, A. Salleo
Department of Materials Science and Engineering
Stanford University
Stanford, CA 94305, USA
E-mail: alexander.giovannitti@chalmers.se; asalleo@stanford.edu

S. A. Hesse, C. J. Tassone, C. J. Takacs
Stanford Synchrotron Radiation Lightsource SLAC National Accelerator Laboratory
Menlo Park, CA 94025, USA

I. McCulloch
Department of Chemistry University of Oxford
Oxford OX1 3TA, UK

A. Giovannitti
Department of Chemistry and Chemical Engineering
Chalmers University of Technology
Göteborg SE-412 96, Sweden

While high carrier mobilities and capacitances are desirable for enabling high-performance bioelectronic devices, the operational stability of OMIECs is also critically important and often overlooked. Stability is often defined from an operational standpoint and thus can have many meanings depending on the device requirements and desired application. For example, the stability of charge transport pathways or polymer morphology may be of less concern in applications like energy storage or electrochromics, where the active material acts as an electrode rather than a transistor. Functional stability and materials stability may thus be distinct. OMIEC stability is commonly investigated through repeated cyclic voltammograms (CVs) or doping/dedoping of OECTs. CVs can show if capacitive charging is stable and determine the existence of instabilities, such as faradaic side reactions which can be evidence of chemical degradation.[8–10] CVs however do not probe directly charge transport or morphological stability. Conversely, repeated OECT operation can detect changes in conductivity, but transfer curves are sensitive to a multitude of factors that cannot be easily separated such as structural disorder, mesoscale connectivity, and the accessibility of electrochemically active sites.

Even in the absence of faradaic side reactions, performance degradation in polymeric OMIEC-based devices has been linked to volume changes and structural degradation from repeated doping/dedoping cycles. The charge densities reached in electrochemical doping are significantly higher than those reached in field effect devices ($\approx 10^{20}$ versus $\approx 10^{19}$ cm^{-3}), and, as a result, the accompanying ionic flux moving into and out of the material is substantial. In aqueous electrolytes, counterions penetrating the semiconductor can bring a hydration shell of water molecules with them,[11,12] leading to large volume changes (i.e., swelling) and potential thin film delamination.[13,14] Indeed, material swelling and mechanical stability are heavily dependent on side chain polarity,[15,16] where long polar side-chains can lead to complete film dissolution[17,18] and the introduction of nonpolar alkyl groups into side chains can limit swelling and improve film adhesion to the substrate.[19] There are thus two distinct but not separable sources of instability: electronic charge density on the conjugated backbone and insertion/expulsion of ions dressed with solvent molecules. Finally, poor device or material stability can also arise from low molecular weight batches of OMIEC materials, though the mechanical degradation often associated with low molecular weight materials limits meaningful material characterization.[20] As any application of OMIECs will ultimately be limited by device stability, understanding the origins of degradation is of great practical importance.

In the present work, we use a suite of characterization techniques to identify the origin of instabilities of an OMIEC molecular weight series in electrochemical transistors. Our findings show that operating OMIECs at high charge densities harms electronic charge transport in these materials by irreversibly decreasing hole mobility. Using *operando* X-ray scattering, we examine the microstructural rearrangements which occur during electrochemical charging and find a strong correlation between drop of the hole mobility and structural disruptions within the crystallites. Thus, while charge carriers initially induce order within the crystallites at low charge densities – below the carrier density where polarons strongly interact – further increases to carrier density leads to a structural disordering of the crystallites, irreversibly decreasing conductivity and mobility. Together, our results provide a crucial link between the structural dynamics of OMIEC materials as a function of charge density, and the stability and performance of electrochemical devices.

2. Results and Discussion

2.1. Structural Characterization

We use a polythiophene homopolymer, p(g3T2), which consists of a 3,3′-dialkoxybithiophene repeat unit with triethylene glycol side chains as shown in **Figure 1a**. In comparison to more structurally complex donor–acceptor copolymers, the chemical structure of these homopolymers is well-defined as the symmetric repeat unit limits homocoupling and regioregularity defects.[21] To isolate possible effects of molecular weight on stability, the material was fractionated using recycling preparative high performance liquid chromatography (HPLC) with a size exclusion column for polymers to generate a total of 4 fractions of different molecular weights (Figure 1a). This procedure not only separates the material by molecular weight, but also acts to remove trace metals and residual catalyst from synthesis, which has been shown to impact the performance of OMIECs (Table S1, Supporting Information).[22] Polymer chains with the highest molecular weight are eluted in the first fraction (F1), whereas shorter chains were eluted in the last fraction (F4), as confirmed by matrix assisted laser desorption ionization time of flight (MALDI-ToF) mass spectrometry (Figure S1, Supporting Information). ^{1}H nuclear magnetic resonance (NMR) spectroscopy was also used to verify the chemical structure of the different fractions were identical (Figure S2, Supporting Information), and thin film optical absorbance was used to verify that the aggregation of the fractions were similar (Figure S3 and Table S2, Supporting Information).

Grazing incidence wide-angle X-ray scattering (GIWAXS) was employed to investigate the microstructure the different molecular weights. Well-defined scattering peaks characteristic of a semicrystalline microstructure were observed in all p(g3T2) fractions. Lamellar (100) peaks indicate ordering along the side-chain stacking direction, π-stacking (010) peaks indicate ordering arising from intermolecular π-orbital interactions, and the backbone (001) peaks indicate ordering of conjugated backbones arising from chain-to-chain registry along the chain axis. While all materials display a semicrystalline microstructure, the different fractions yield changes in crystalline texture (Figure 1b). F3 is predominantly edge-on, while F1, F2, and F4 are face-on, with the latter two fractions showing some mixed character. These texture changes are likely due to crystallization kinetics during the spin-coating process and may arise from a multitude of factors including the viscosity of polymer solutions, changes in polymer solubility, and aggregation effects in solution—all of which are strongly impacted by molecular weight.[23–25] These changes in film texture are evident in the GIWAXS lineouts where the preferential orientation of the crystallites can be seen (Figure 1c,d). In agreement with literature, the more thermodynamically stable edge-on crystallites, found more abundantly in F3 and F4, exhibit smaller lamellar spacings than the face-on crystallites (Table S3, Supporting Information).[26,27] As expected, these denser crystallites also exhibit increased small-angle scattering intensity

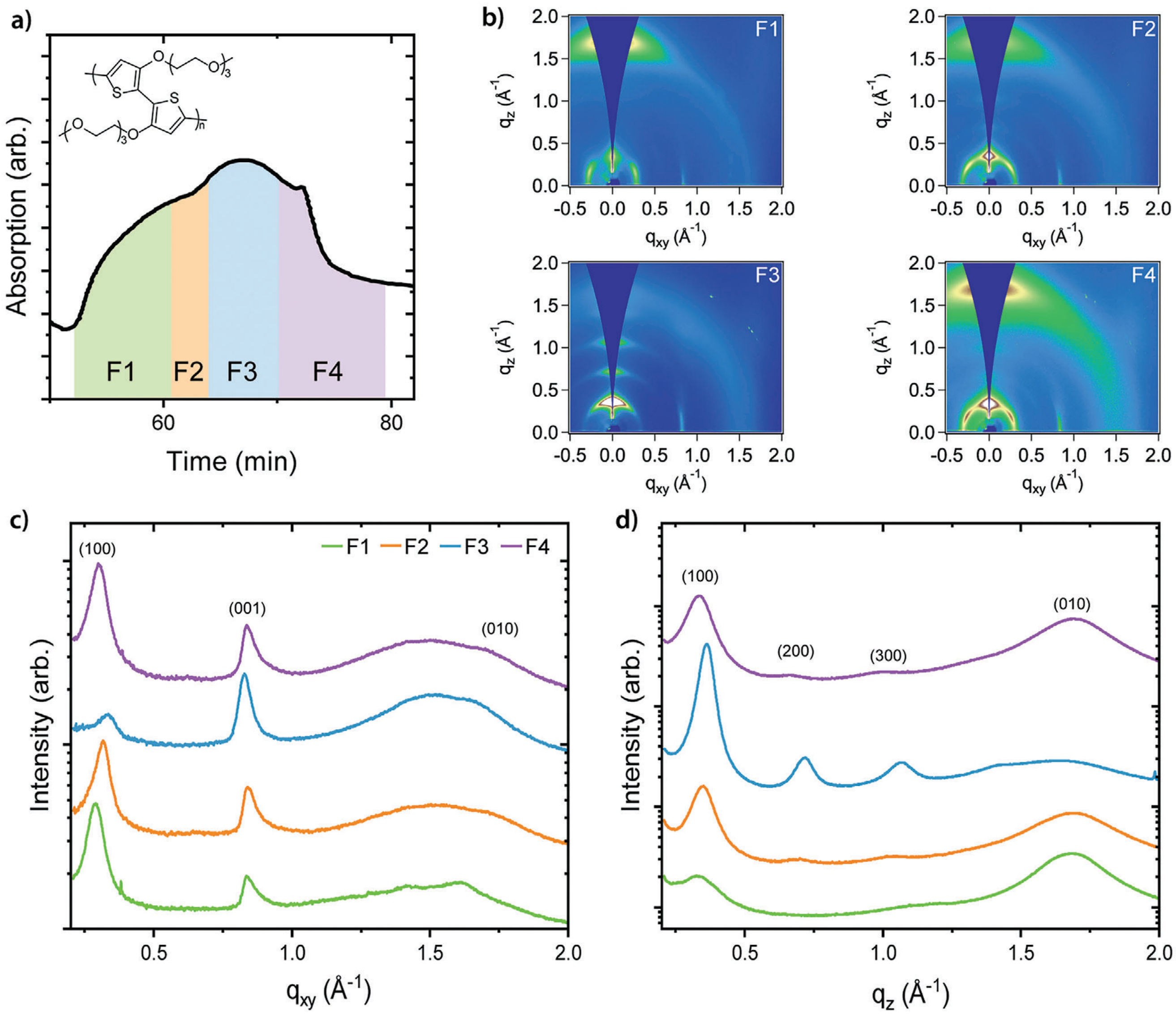

Figure 1. Ex situ structural characterization of dry fractionated p(g3T2) films. a) Recycling HPLC trace showing the separation of different fractions (2nd cycle). b) 2D GIWAXS patterns of the fractioned polymer (F1–F4). c) In-plane and d) out-of-plane X-ray scattering lineouts. GIWAXS lineouts are offset for clarity and peak labels are shown on the top trace.

(Figure S4, Supporting Information). Lastly, it is interesting to note that the texture and lineouts of F3, the fraction from the center of the recycling HPLC trace, most closely resemble that of the as-received material (Figure S5, Supporting Information).

2.2. Charge Density Dependence on OECT Stability

OECTs were fabricated to investigate the operational stability of the different molecular weight polymers in electrochemical devices. The conductivity changes measured in a transfer curve are a function of both the number of charges injected into the material under the applied gate voltage as well as the mobility of each of those charge carriers. To separate these factors, OECTs were operated in a bipotentiostat configuration which performs simultaneous CVs at source and drain electrodes, with a small potential offset (V_{SD} = 10 mV) between the electrodes.[28] Due to the small source-drain bias, the doping state experienced across the channel is essentially constant and the OECT operates in the linear regime. Although this regime results in lower transconductances,[29] the simultaneous measurement of conductivity, σ, and carrier density, ρ, enables mobility, μ, to be determined as a function of electrochemical potential and is thus better suited to fundamental transport studies. In the present work, we use the term differential mobility, $d\mu = d\sigma/(ed\rho)$ to refer to the mobility of newly added charge carriers, whereas the mobility, $\mu = \sigma/(e\rho)$, refers to the average mobility of all carriers (see Note S1 in the Supporting Information for details).

The transfer curves of the various fractions (**Figure 2a**) show a clear separation in conductivity between the two highest

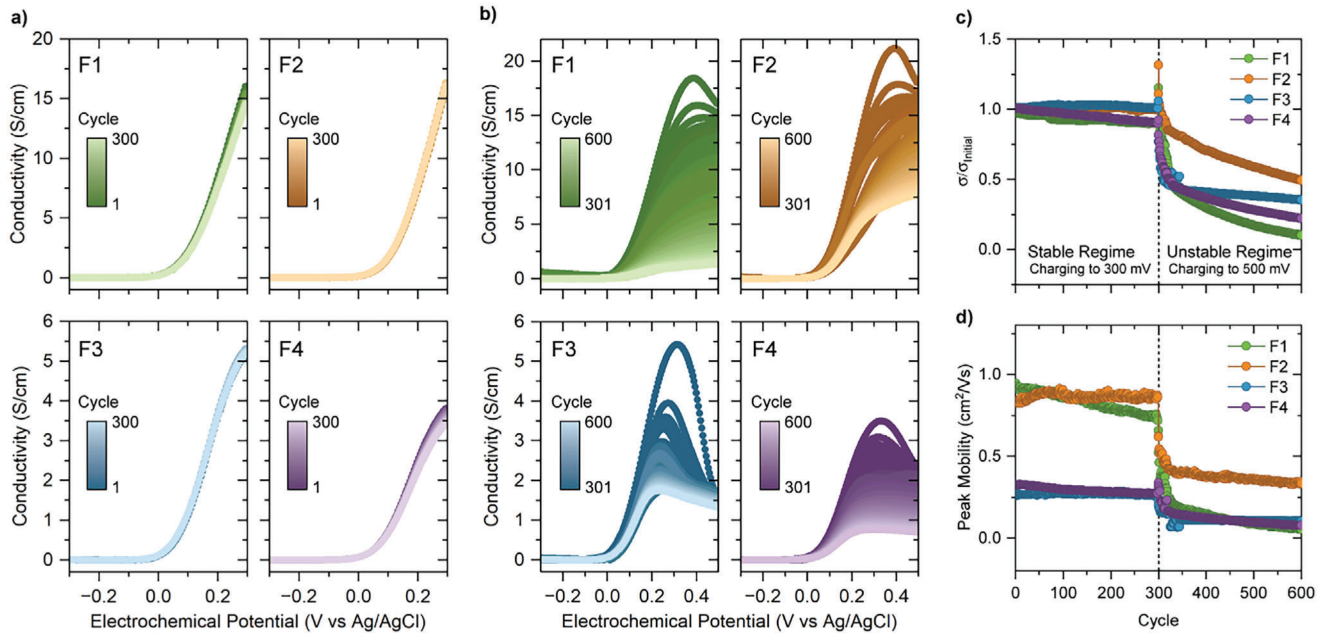

Figure 2. OECT characterization of fractionated materials. Transfer curves measured up to a) 300 mV and b) 500 mV versus Ag/AgCl with 0.1 м NaCl as the electrolyte. The cycle number is given by the colorbar inset in each panel, and only the forward scans are shown for clarity. OECT channels were 2 mm × 200 µm (width × length) and the V_{SD} was 10 mV. c) Normalized maximum conductivity and d) maximum differential mobility versus cycle for all fractions, showing the stable and unstable regimes of operation.

molecular weight fractions (F1 and F2) and the lowest molecular weight fractions (F3 and F4). This observation suggests that F1 and F2 are above the critical molecular weight required to form a well-connected microstructure of crystallites joined by tie-chains, whereas in F3 and F4 shorter polymer chains result in poor electronic mobilities due to a lack of such microstructural connection. These measurements highlight the importance of polymer chain length on the operation of OMIEC materials: high carrier mobility requires fast in-chain transport within crystallites concomitant with sufficient connectivity provided by tie chains.[30–32]

We find that the operational stability of the materials strongly depends on the electrochemical potential upon oxidation, and hence the maximum charge density that the film experiences, and is largely irrespective of molecular weight. When charged to 300 mV versus Ag/AgCl, the transfer curves of all fractions are stable across 300 cycles indicating reversible electrochemical charging with little changes to charge transport pathways (Figure 2a). In this stable regime, the polymer is charged to just below the point of maximum conductivity, and we estimate there to be ≈0.14–0.18 charge/monomer (Figure S6, Supporting Information), where a monomer is comprised of two thiophene rings (Figure 1a). We note that the carrier densities calculated for F4 are consistently less than those of the other fractions; we believe this to be an artifact due to partial dissolution of the material upon electrolyte exposure as a result of the low molecular weight (Note S2, Supporting Information). In this lower carrier density regime (i.e., <300 mV versus Ag/AgCl) the mean hole mobility increases as charge carriers are added. However, when moving to higher carrier densities on the first charging cycle to 500 mV versus Ag/AgCl, the conductivity peaks and then decreases as the electrochemical potential is further increased (Figure 2b), exhibiting a negative transconductance. This decrease in conductivity indicates a decrease in the mean mobility of all charge carriers; thus, the addition of holes at these higher charge densities decreases the mobility of existing carriers (Figure S7, Supporting Information). In F1–F3, the carrier density at which this occurs is between 0.15 and 0.25 charges/monomer, or ≈1 charge per 8–13 thiophene rings. This decrease in mobility at greater charge densities is accompanied by a striking increase in hysteresis (Figure S8, Supporting Information).

Upon repeated cycling to more oxidizing potentials (500 mV versus Ag/AgCl), the transfer curves of the materials are unstable, and the conductivities decrease from their initial values with each biasing cycle (Figure 2b). Despite these changes to the transfer curves, the simultaneously measured CVs are very stable (Figure S9, Supporting Information), meaning that faradaic side reactions or loss of capacitance cannot explain the changes. We thus deduce that the conductivity rapidly decreases due to diminishing hole mobility (Figure 2d). The optical absorption of the materials also remains remarkably consistent both before and after repeated cycling to 500 mV versus Ag/AgCl (Figure S10, Supporting Information), indicating that short-range structural order of aggregates and the amount of amorphous regions are not dramatically impacted by charging the film to higher potentials. Thus, optical and electrochemical characterization using CVs do not reveal any of the dramatic instabilities observed in OECTs.

2.3. Structural Evolution During Electrochemical Doping

The decrease in carrier mobility while volumetric capacitance and material short-range ordering remain unaffected suggests

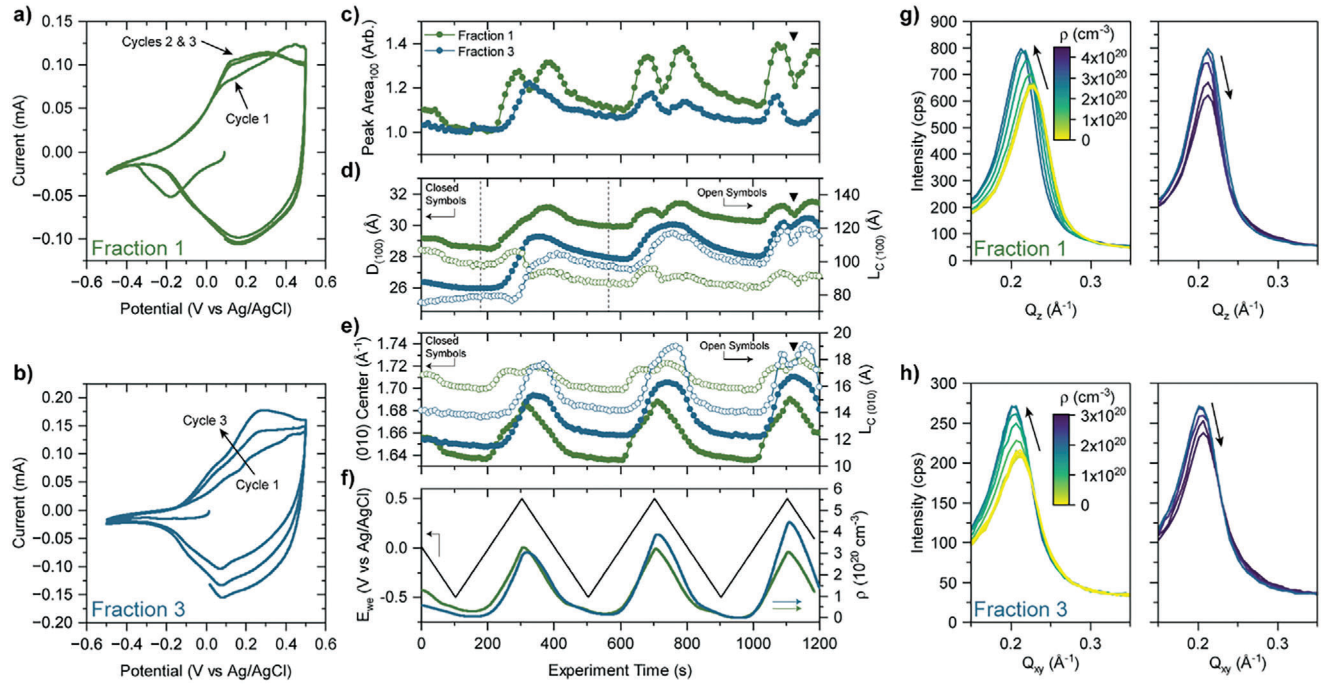

Figure 3. *Operando* cyclic voltammograms of a) a high molecular weight fraction (F1), and b) a low molecular weight fraction (F3) in 0.1 м NaCl. c–e) Fit results from X-ray scattering peaks of F1 (green) and F3 (blue). The start and end of the first CV cycle is shown by the dotted lines in panel (d). The ▼ symbol indicates the change in structural behavior at high charge densities. f) Electrochemical data measured during the *operando* X-ray scattering experiment. g,h) Lineouts of the lamellar stacking peak of F1 and F3 during the forward scan of the 3rd cycle of the CV, with (left) low carrier densities and (right) high carrier densities shown separately for clarity and to highlight the position inversion. The lineouts for each fraction are color-coded to the carrier density, shown by the colorbar inset.

that the irreversible changes at high charge densities arise from longer-range microstructural effects. To investigate such structural changes, we used *operando* GIWAXS to characterize the structure of the polymer during operation while avoiding parasitic currents and faradaic side reactions. The latter is crucial as it allows us to unequivocally link microstructural changes to the carrier density in the organic semiconductor and to transport properties (Figure 2). As a result, all our structural and transport measurements are consistent with the elctrochemistry we measure ex situ. F1 and F3 were chosen as representative examples of materials falling in two different regimes of crystalline texture, carrier mobility, and overall OECT performance. We thus henceforth restrict our study to these two materials.

Upon electrolyte exposure (0.1 м NaCl) but prior to biasing, the crystallites spontaneously expand by ≈7 Å in the lamellar direction as the side-chains swell with water molecules and ions (Figure S11, Supporting Information).[33] *Operando* CVs were then performed to track the structure of the material during the first 3 oxidation and reduction cycles of these films (**Figure** 3a,b). For both F1 and F3, charging of the polymer results in an expansion in the lamellar stacking distance (Figure 3d). Upon discharging, only some of this lamellar strain is recovered, meaning that the first charge–discharge cycle, denoted by the dotted lines in Figure 3d, results in a permanent expansion of the crystallites (1.4 Å for F1 and 1.9 Å for F3). This irreversible expansion from "active swelling" of the crystallites is surprisingly analogous to the hydration of side-chain free polymers like BBL,[34] highlighting the ubiquity of electrochemically driven hydration in OMIEC materials. Interestingly, evidence of these first cycle irreversibility can also be found in the CVs where the peak current occurs at greater electrochemical potentials in the first cycle, indicating that more electrochemical work was required to charge the polymer during the first scan.

We now turn our attention to the latter two cycles of the *operando* CVs. F3 exhibits some "break-in" where the current increases upon subsequent cycles (Figure 3b), indicating that more of the film is electrochemically accessible. Indeed, the CV behavior provides context for the continued change in structure upon charging, highlighting the importance of being able to quantify injected charge and thus carrier density during in situ and *operando* experiments in order to correctly interpret the effect of charge on structure (Figure S12, Supporting Information). By the third cycle, this "break-in" is largely completed and the CV resembles that of ex situ experiments. During charging, the π-stacking distance in both F1 and F3 contracts and the coherence length increases, indicating ordering along this stacking direction. This is accompanied by a simultaneous increase in intrachain exciton coupling (Figures S13 and S14, Note S3, Supporting Information), meaning the newly bleached chains where newly added charges reside are predominantly in aggregate regions and are becoming increasingly more planar. The combination of increased order along the π-stacking direction and simultaneous planarization of neutral chains indicates that the presence of charge carriers planarizes polymer backbones within the crystallites, which enables them to pack more closely with less disorder. This mechanism was first observed in the electrochemical charging of p(g2T-TT) in ionic liquid where crystallites were found to dynamically order upon charging.[35] This dynamic ordering provides a structural basis for the reversible rise in carrier mobility with charge density. We thus conclude that this dynamic ordering phenomenon is independent of electrolyte screening and ionic strength and is a general property of redox-active conjugated polymers.

At higher charge densities, we observe a distinct change in structural behavior: the intensity, spacing, and coherence length of the lamellar stacking peak simultaneously decrease (Figure 3c–e, ▼ symbol). The onset of this change occurs close to 300 mV versus Ag/AgCl, revealing that the irreversible mobility degradation observed in OECT measurements is linked to these structural changes within the crystallites (Figures S15 and S16, Supporting Information). Evidence of this structural disruption is also found in the crystalline directions responsible for charge transport, namely the π-stacking and backbone directions. The π-stacking, or (010), peak decreases in intensity and its coherence length slightly decreases. Similarly, the "backbone" peak at ≈0.8 Å^{-1} rapidly decreases in intensity (Figure S17, Supporting Information), which signals a disruption of the chain-to-chain registry within the crystallites. Because it is caused by chain-to-chain registry, the backbone peak is a sensitive probe of crystalline order.[36]

The onset of structural disruptions and concurrent decrease in hole mobility occur at carrier densities where the area/charge approaches the expected size of a polaron in these materials (Note S4, Supporting Information),[37–41] leading us to suspect that charge-charge interactions (such as bipolaron formation or polaron–polaron interactions) are responsible. Spectroelectrochemical measurements show a decrease in polaronic absorption and general change in polaron spectral shape at more anodic potentials (>0.25 V versus Ag/AgCl), supporting the presumption that at high potentials the simple picture of neutral chains being progressively populated by polarons breaks down and that interactions between polarons become relevant (Figure S13, Supporting Information). We hypothesize that such polaronic interactions increase the localization of charges (consistent with decreased hole mobility), giving rise to the maximum in mobility and transconductance prior to their occurrence. Indeed, it is possible that strong coulombic interactions between holes may lead to the opening of a coulomb gap in the polaron density of states that results in a band of low mobility charges,[42] in line with work on electrochemically gated[43,44] and ion-exchange doped polymers[45] at high carrier densities. It should be noted that electrochemically gated poly(alkylthiophene) derivatives also show an analogous peak in hole mobility at similar charge densities (one hole per ≈7–10 thiophene rings),[46,47] suggesting this behavior is not specific to OMIECs in particular but rather conjugated polymers in general. We also emphasize that the delineation between two strongly coupled polarons and a bipolaron is nontrivial as the spectral signatures of these species are still debated.[48,49] Nevertheless, the present results show that at low carrier densities (when charges do not strongly interact) polarons induce order within the crystallites and enhance transport. On the other hand, at high charge densities (when polarons strongly interact) significant structural perturbations occur within the crystallites which permanently disrupt charge transport. For the purposes of stable OMIEC device operation, excessive charge densities should be avoided to minimize such effects. We note that such "over-oxidation" is damaging due to structural effects rather than chemical degradation as the optical absorption of the material remains unchanged.

2.4. Structural and Electronic Hysteresis Resulting from Charge–Charge Interactions

Having identified structural perturbations associated with high electronic charge densities in the materials, we measured *operando* OECT transfer curves to investigate the structural and electronic reversibility of these effects. The electrochemical potential of the films was stepped from a reduced state (−0.2 V versus Ag/AgCl) to an oxidized state (0.6 V versus Ag/AgCl) while applying a 50 mV bias between the source and drain contacts to measure channel conductivity. The *operando* transfer curves measured at the beamline, shown in **Figure 4**, are in agreement with ex situ transfer curves, showing similar thresholds, conductivity, and even the hysteresis noted previously (Figure S8, Supporting Information). This hysteresis in conductivity arises from a hysteresis in carrier mobility where charges are less mobile on the reverse scan once high carrier densities have been reached (Figure 4a,b). This drop in conductivity and increased hysteresis is again consistent with the conversion of polarons into less-mobile species such as bipolarons or strongly coupled polarons.[50,51] The electronic hysteresis is accompanied by a structural hysteresis in the coherence length (L_c) of the lamellar stacking (100) peak (Figure 4c,d). The coherence length initially increases up to 300 mV versus Ag/AgCl as polarons induce structural order within the crystallites, but then decreases at more positive potentials when higher carrier densities are reached. There are also two contractions to the lamellar spacing which occur during charging (Figure 4e,f). The first occurs at ≈−100 mV versus Ag/AgCl and is consistent with cation expulsion from the crystallites.[52,53] The second more pronounced contraction follows the lamellar expansion upon doping and coincides with when the lamellar coherence length and channel conductivity decrease. Thus, the onset of strong charge–charge interactions in the material gives rise to a structural disordering and contraction of the crystallites. This contraction is reversible, but the disordering which occurs at high carrier densities is largely retained on the reverse scan of the transfer curve, resulting in permanent disruptions to the crystalline order and providing a structural basis for the rapid degradation of carrier mobility and film conductivity seen in the stress cycling of OECTs (Figure 2b). This permanent disruption and quartz crystal microbalance measurements lead us to exclude cation expulsion as the origin of this lattice contraction at high anodic potentials.[52,53] A molecular weight dependence on the hysteresis is also observed where F1 shows less electronic and structural hysteresis compared to F3 (Figure 4; Figure S8, Supporting Information). This observation is consistent with the OECT measurements which showed that the higher molecular weights (i.e., F1 and F2) could sustain greater charge densities before mobility decreases (Figure S7, Supporting Information). Together, these results suggest that longer chains could make crystallites more resilient to the structural disruptions which degrade charge transport pathways, but conclusive evidence would require a suite of materials to be investigated.

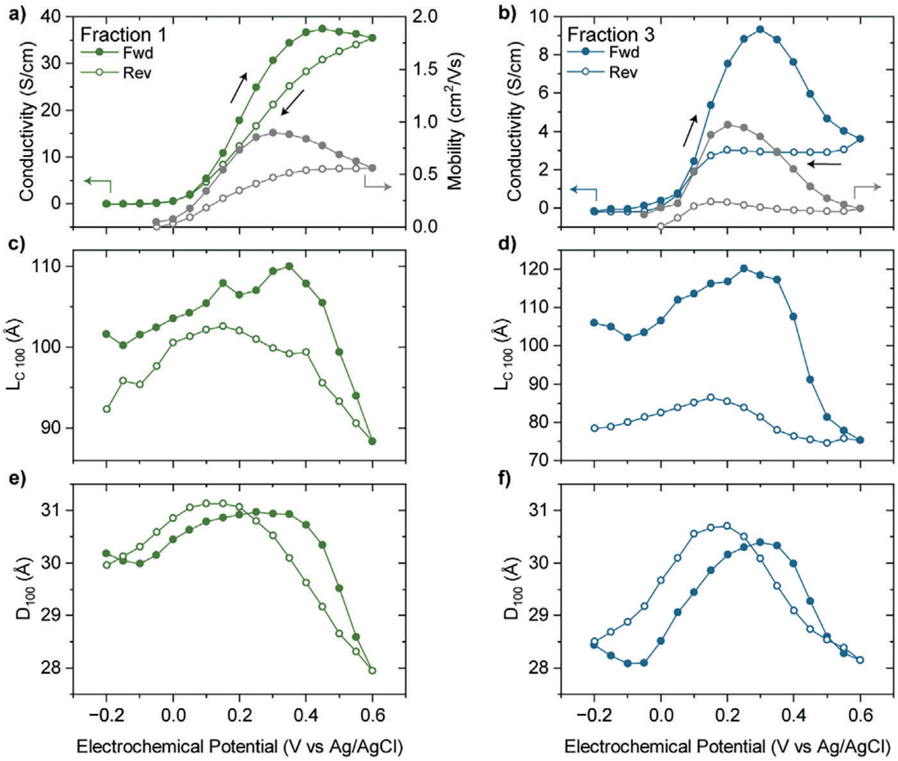

Figure 4. *Operando* OECT transfer curves of p(g3T2) with $V_D = 50$ mV in 0.1 M NaCl. Transfer curves and mean mobility for a) F1 and b) F3. Lamellar coherence length from the Scherrer equation for c) F1 and d) F3. Lamellar spacing for e) F1 and f) F3. The forward scan is shown with closed symbols and the reverse scan is shown with open symbols. The black arrows in the top panels indicate the direction of the scan.

The observed decreases in crystalline order at high carrier densities are consistent with recent work based on time dependent density functional theory calculations on P3HT which suggested that as carrier density is increased polarons will first strongly couple and eventually spin-pair to form bipolarons.[49] There, the presence of bipolarons coincided with a decrease in P3HT crystallinity, and we observe a similar decrease in relative degree of crystallinity (rDOC) after charging and discharging the polymer (Figure S18, Supporting Information). Hence, our findings suggest that structural rearrangements necessary to stabilize high charge densities in the crystalline domains permanently disrupt the long-range ordering of the material. For example, while counterions have been reported to reside close to the mid-lamellae of OMIECs,[54] it is possible that counterion positions change at higher charge densities to properly solvate and stabilize multicharge complexes.[48,49] While crystalline coherence length is affected by electrochemical charging to high carrier density, changes to the lamellar spacing are more reversible, with peak positions reaching values after discharging that are close to those measured when first exposing the polymer to the electrolyte. Thus, it appears unlikely that the accumulation of ions or water molecules in the crystallites accounts for the polymer's structural instability, because such accumulation would result in a permanent expansion of the crystallites. Rather, such water accumulation is expected to be localized in amorphous regions and thus cannot account for the degradation of crystalline domains.[12] This is confirmed by measuring F1 of p(g3T2) in the ionic liquid 1-Ethyl-3-methylimidazolium ethyl sulfate (EMIM:EtSO4) where the same degradation in hole mobility and increased hysteresis is observed in the absence of solvent molecules (Figure S19, Supporting Information). Thus, the possible accumulation of water or solvent molecules cannot account for the degradation of charge transport or increased disorder in the crystalline domains. Our data thus strongly suggests that the structural instabilities we observe in p(g3T2) crystallites at high oxidation potential are caused by backbone distortions originating from the high charge density in the conjugated core rather than by "erosion" of crystalline order caused by ingress of solvent molecules. This degradation is thus a fundamental consequence of the strong electron-lattice coupling in organic semiconductors.

3. Conclusion

In the present work, we provide a direct link between the carrier density in OMIECs and the resulting electronic and microstructural stability. We show that electronic transport and electrochemical charging of a prototypical OMIEC material at various molecular weights are stable when high carrier densities are avoided. However, when repeatedly charged to carrier densities exceeding ≈0.14 – 0.18 charges/monomer (or 1 charge per 11–14 thiophene rings), irreversible decreases in conductivity and increased hysteresis are observed. We show that this decrease in conductivity results from a drop in hole mobility and appears irrespective of molecular weight. *Operando* X-ray scattering measurements further reveal that irreversible structural disruptions occur within the crystallites at high carrier densities, providing a structural basis for the degradation of mobility, and increased hysteresis. The onset of this structural disordering coincides with carrier densities where polarons are likely to strongly interact with one another, suggesting that coupled polarons, bipolaron formation, or other multicharged complexes and the structural deformations that they induce are the reason for the observed microstructural instabilities rather than mechanical strain caused by the insertion of solvated ions. The findings suggest on one hand that OECTs should be operated at low carrier densities where microstructural changes are reversible, highlighting the importance of developing polymers that achieve high mobilities at low carrier densities. On the other hand, our findings indicate that engineering the molecular structure of the polymer (e.g., more rigid molecules) might mitigate these instabilities and allow stable and reversible high charge-density operation, which is extremely desirable in energy storage applications for instance.

4. Experimental Section

Materials: p(g3T2) was synthesized as previously reported.[55] The material was then separated into different molecular weight fractions as follows. A 5 mg mL^{-1} solution of p(g3T2) was prepared in chloroform, filtered through a 0.45 µm syringe filter and loaded onto the Recycling Preparative HPLC (LaboACE LC-5060) using a glass injection syringe. The polymer was recycled for one cycle and collected into four fractions on the second cycle, where each fraction corresponds to approximately a quarter of the material. Molecular weight measurements were acquired with a Micromass MALDI-ToF using matrix-assisted laser desorption ionization (MALDI) techniques on linear acquisition operation mode and a positive voltage polarity, using trans-2-[3-(4-*tert*-butylphenyl)−2-methyl-2-propenylidene]-malononitrile (DCTB) as the matrix.

OECT Measurements: OECT devices (channel dimensions of width = 2 mm and length = 200 µm) were lithographically patterned using a dry peel-off method described previously.[56] Device thicknesses were characterized with a Bruker Dektak profilometer. OECTs were characterized with a bipotentiostat with two working electrodes (connected to the source and drain electrodes of the OECT), a counter electrode (Pt wire), and a reference electrode (leakless Ag/AgCl from eDAQ) using an Ar sat. 0.1 M NaCl aqueous solution. Detailed information regarding has been provided in previous work.[57]

Ex Situ Grazing Incidence Wide-Angle X-ray Scattering: Grazing incidence wide-angle X-ray scattering was performed at the Stanford Synchrotron Radiation Lightsource on beamline 11–3 at an incidence energy of 12.7 keV and collected using an area detector (Rayonix MAR-225). The distance between sample and detector was calibrated using a LaB6 polycrystalline standard. The incidence angle (0.1°) was slightly larger than the critical angle of Si. GIWAXS raw data was corrected for the geometric distortion introduced by a flat, plate detector, normalized by detector counts and film thickness, and reduced and analyzed using a combination of Nika 1D SAXS and WAXStools software packages in Igor Pro.[58,59]

Operando Grazing Incidence Wide-Angle X-ray Scattering: Porous ceramic substrates (Newark) were cleaned in acetone and polished by hand on a Buehler grinding and polishing wheel. Gold contacts were evaporated onto the frits using a thermal evaporator in a nitrogen glovebox. p(g3T2) films were prepared by drop casting polymer solutions from chloroform (10 mg mL^{-1}) onto a sacrificial layer of Poly(diallyldimethylammonium chloride) (Sigma Aldrich). The films were lifted off the sacrificial layer in water and transferred to the ceramic substrates.

Operando grazing incidence wide-angle X-ray scattering was performed at the Stanford Synchotron Radiation Lightsource on beamline 10–2a at an incident energy of 12 keV and collected using an area detector (EIGER 1M). The collimated incident beam was ≈50 um in height and ≈500 um wide. The distance between the sample and detector was calibrated using LaB6 powder, and the incidence angle was 0.1 or 0.2 degrees, depending on which angle provided the best signal of the polymer. Measurements were performed in a Helium chamber with polycarbonate windows to minimize air scatter and oxygen side-reactions. The X-ray scattering data were reduced in Python using the open-source pyFAI and pygix modules.[60,61] A forked version of the pygix module was used (available at https://github.com/ctakacs/pygix) for compatibility with Python 3. Scattering peaks were fit to Gaussian–Lorentzian lineshapes using the lmfit package in Python 3.7. To isolate the π-stacking peak of F1 for fitting, the isotropic scattering from the substrate (in the q_{xy} direction) was subtracted from the scattering containing the π-stacking peak (in the q_z direction). The isotropic scattering of F3 was not amenable to this background removal process, so an iterative background removal approach was used which is described in Note S5 (Supporting Information).

Electrochemical measurements were taken on a two-channel Biologic SP-300 potentiostat in a three-electrode setup with a leakless Ag/AgCl reference electrode (eDAQ) and a PEDOT:PSS (Clevios PH1000) counter electrode, as described previously.[35] The electrolyte (0.1 M NaCl) was continuously degassed with Helium to minimize side reactions with oxygen. Operando transistor measurements were performed by separately biasing the source and drain electrodes in a bipotentiostat configuration with a source-drain bias of 50 mV. The carrier density was calculated from the injected charge over the course of the CV or transfer curve and film volume. Carrier densities were calculated based on the thickness of the dry film.

Supporting Information

Supporting Information is available from the Wiley Online Library or from the author.

Acknowledgements

T.J.Q. and G.L. contributed equally to this work. The authors wish to acknowledge Kartik Choudary. T.J.Q. and G.L. acknowledge support from the National Science Foundation Graduate Research Fellowship Program under grant DGE-1656518. This material was based on work supported by the US Department of Energy (DOE), Office of Science, Office of Workforce Development for Teachers and Scientists, Office of Science Graduate Student Research (SCGSR) program. The SCGSR program was administered by the Oak Ridge Institute for Science and Education for the DOE under Contract No. DE-SC0014664. A.G. and A.S. acknowledge funding from the TomKat Center for Sustainable Energy at Stanford University. A.S. gratefully acknowledges financial support from the National Science Foundation Award No. DMR 1808401. The use of Stanford Synchrotron Radiation Lightsource, SLAC National Accelerator Laboratory, was supported by the US DOE, Office of Science, Office of Basic Energy Sciences, under contract no. DE-AC02-76SF00515. Part of this work was performed at the Stanford Nano Shared Facilities (SNSF), supported by the National Science Foundation under award ECCS-2026822. A.S. and T.J.Q. acknowledge financial support from the National Science Foundation and the Semiconductor Research Corporation, E2CDA award no. 1739795. I.M. acknowledges financial support from KAUST Office of Sponsored Research CRG10, by EU Horizon2020 grant agreement no. 952911, BOOSTER, grant agreement no. 862474, RoLA-FLEX, and grant agreement no. 101007084 CITYSOLAR, as well as EPSRC Projects EP/T026219/1 and EP/W017091/1. The work at Stanford University was supported as part of the Center for Soft PhotoElectroChemical Systems (SPECS), an Energy Frontier Research Center funded by the U.S. Department of Energy, Office of Science, Basic Energy Sciences under award # DE-SC0023411.

Conflict of Interest

The authors declare no conflict of interest.

Data Availability Statement

The data that support the findings of this study are available from the corresponding author upon reasonable request.

Keywords

electrochemical transistors, microstructural stability, operando X-ray scattering, organic mixed conductors, organic semiconductors

[1] B. D. Paulsen, K. Tybrandt, E. Stavrinidou, J. Rivnay, *Nat. Mater.* **2020**, *19*, 13.
[2] C. Cea, G. D. Spyropoulos, P. Jastrzebska-Perfect, J. J. Ferrero, J. N. Gelinas, D. Khodagholy, *Nat. Mater.* **2020**, *19*, 679.
[3] S. Griggs, A. Marks, H. Bristow, I. Mcculloch, *J. Mater. Chem. C* **2021**, *9*, 8099.
[4] X. Chen, A. Marks, B. D. Paulsen, R. Wu, R. B. Rashid, H.u Chen, M. Alsufyani, J. Rivnay, I. Mcculloch, *Angew. Chem., Int. Ed.* **2021**, *60*, 9368.
[5] A. Giovannitti, D.-T. Sbircea, S. Inal, C. B. Nielsen, E. Bandiello, D. A. Hanifi, M. Sessolo, G. G. Malliaras, I. Mcculloch, J. Rivnay, *Proc. Natl. Acad. Sci. USA* **2016**, *113*, 12017.
[6] G. Garcia-Belmonte, J. Bisquert, E. C. Pereira, F. Fabregat-Santiago, *J. Electroanal. Chem.* **2001**, *508*, 48.
[7] M. Moser, T. C. Hidalgo, J. Surgailis, J. Gladisch, S. Ghosh, R. Sheelamanthula, Q. Thiburce, A. Giovannitti, A. Salleo, N. Gasparini, A. Wadsworth, I. Zozoulenko, M. Berggren, E. Stavrinidou, S. Inal, I. Mcculloch, *Adv. Mater.* **2020**, *32*, 2002748.
[8] A. Giovannitti, R. B. Rashid, Q. Thiburce, B. D. Paulsen, C. Cendra, K. Thorley, D. Moia, J. T. Mefford, D. Hanifi, D.u Weiyuan, M. Moser, A. Salleo, J. Nelson, I. Mcculloch, J. Rivnay, *Adv. Mater.* **2020**, *32*, 1908047.
[9] A. De La Fuente Durán, A. Yu-Lun Liang, I. Denti, H. Yu, D. Pearce, A. Marks, E. Penn, J. Treiber, K. Weaver, L. Turaski, I. P. Maria, S. Griggs, X. Chen, A. Salleo, W. C. Chueh, J. Nelson, A. Giovannitti, J. T. Mefford, *Preprint* **2023**, *16*, 5409.
[10] S. Zhang, P. Ding, T. P. Ruoko, R. Wu, M. A. Stoeckel, M. Massetti, T. Liu, M. Vagin, D. Meli, R. Kroon, J. Rivnay, S. Fabiano, *Adv. Funct. Mater.* **2023**, *33*, 2302249.
[11] A. Savva, C. Cendra, A. Giugni, B. Torre, J. Surgailis, D. Ohayon, A. Giovannitti, I. McCulloch, E. Di Fabrizio, A. Salleo, J. Rivnay, S. Inal, *Chem. Mater.* **2019**, *31*, 927.
[12] L. Q. Flagg, C. G. Bischak, J. W. Onorato, R. B. Rashid, C. K. Luscombe, D. S. Ginger, *J. Am. Chem. Soc.* **2019**, *141*, 4345.
[13] A. A. Szumska, I. P. Maria, L. Q. Flagg, A. Savva, J. Surgailis, B. D. Paulsen, D. Moia, X. Chen, S. Griggs, J. T. Mefford, R. B. Rashid, A. Marks, S. Inal, D. S. Ginger, A. Giovannitti, J. Nelson, *J. Am. Chem. Soc.* **2021**, *143*, 14795.
[14] L. Q. Flagg, L. E. Asselta, N. D'Antona, T. Nicolini, N. Stingelin, J. W. Onorato, C. K. Luscombe, R. Li, L. J. Richter, *ACS Appl. Mater. Interfaces* **2022**, *14*, 29052.
[15] M. Moser, L. R. Savagian, A. Savva, M. Matta, J. F. Ponder, T. C. Hidalgo, D. Ohayon, R. Hallani, M. Reisjalali, A. Troisi, A. Wadsworth, J. R. Reynolds, S. Inal, I. Mcculloch, *Chem. Mater.* **2020**, *32*, 6618.
[16] Y. Wang, E. Zeglio, H. Liao, J. Xu, F. Liu, Z. Li, I. P. Maria, D. Mawad, A. Herland, I. Mcculloch, W. Yue, *Chem. Mater.* **2019**, *31*, 9797.
[17] A. A. Szumska, I. P. Maria, L. Q. Flagg, A. Savva, J. Surgailis, B. D. Paulsen, D. Moia, X. Chen, S. Griggs, J. T. Mefford, R. B. Rashid, A. Marks, S. Inal, D. S. Ginger, A. Giovannitti, J. Nelson, *J. Am. Chem. Soc.* **2021**, *143*, 14795.
[18] J. Gladisch, E. Stavrinidou, S. Ghosh, A. Giovannitti, M. Moser, I. Zozoulenko, I. Mcculloch, M. Berggren, *Adv. Sci.* **2020**, *7*, 1901144.
[19] Y. He, N. A. Kukhta, A. Marks, C. K. Luscombe, *J. Mater. Chem. C* **2022**, *10*, 2314.
[20] B. T. Ditullio, L. R. Savagian, O. Bardagot, M. De Keersmaecker, A. M. Österholm, N. Banerji, J. R. Reynolds, *J. Am. Chem. Soc.* **2023**, *145*, 122.
[21] D. A. Warr, L. M. A. Perdigão, H. Pinfold, J. Blohm, D. Stringer, A. Leventis, H. Bronstein, A. Troisi, G. Costantini, *Sci. Adv.* **2018**, *4*, 0.
[22] S. Griggs, A. Marks, D. Meli, G. Rebetez, O. Bardagot, B. D. Paulsen, H.u Chen, K. Weaver, M. I. Nugraha, E. A. Schafer, J. Tropp, C. M. Aitchison, T. D. Anthopoulos, N. Banerji, J. Rivnay, I. Mcculloch, *Nat. Commun.* **2022**, *13*, 7964.
[23] J. Deng, L. Zheng, C. Ding, Y. Guo, Y. Xie, J. Wang, Y. Ke, M. Li, L. Li, R. A. J. Janssen, *Adv. Funct. Mater.* **2022**, *33*, 2209195.
[24] B. Mcculloch, V. Ho, M. Hoarfrost, C. Stanley, C. Do, W. T. Heller, R. A. Segalman, *Macromolecules* **2013**, *46*, 1899.
[25] H. Sirringhaus, P. J. Brown, R. H. Friend, M. M. Nielsen, K. Bechgaard, B. M. W. Langeveld-Voss, A. J. H. Spiering, R. A. J. Janssen, E. W. Meijer, P. Herwig, D. M. De Leeuw, *Nature* **1999**, *401*, 685.
[26] S. Y. Son, T. Park, W. You, *Chem. Mater.* **2021**, *33*, 4541.
[27] M. T. Seifrid, S. D. Oosterhout, M. F. Toney, G. C. Bazan, *ACS Omega* **2018**, *3*, 10198.
[28] C. Karlsson, H. Huang, M. Strømme, A. Gogoll, M. Sjödin, *Electrochim. Acta* **2015**, *179*, 336.
[29] P. R. Paudel, V. Kaphle, D. Dahal, R. K. Radha Krishnan, B. Lüssem, *Adv. Funct. Mater.* **2021**, *31*, 2004939.
[30] K. Gu, C. R. Snyder, J. Onorato, C. K. Luscombe, A. W. Bosse, Y.-L. Loo, *ACS Macro Lett.* **2018**, *7*, 1333.
[31] R. Noriega, J. Rivnay, K. Vandewal, F. P. V. Koch, N. Stingelin, P. Smith, M. F. Toney, A. Salleo, *Nat. Mater.* **2013**, *12*, 1038.
[32] H.-Y. Wu, C.-Y. Yang, Q. Li, N. B. Kolhe, X. Strakosas, M.-A. Stoeckel, Z. Wu, W. Jin, M. Savvakis, R. Kroon, D. Tu, H. Y. Woo, M. Berggren, S. A. Jenekhe, S. Fabiano, H.-Y. Wu, C.-Y. Yang, Q. Li, X. Strakosas, M.-A. Stoeckel, W. Jin, M. Savvakis, R. Kroon, D. Tu, M. Berggren, S. Fabiano, *Adv. Mater.* **2021**, *34*, 2106235.
[33] R. Wu, B. D. Paulsen, Q. Ma, J. Rivnay, *ACS Appl. Mater. Interfaces* **2023**, *15*, 30553.
[34] J. Guo, L. Q. Flagg, D. K. Tran, S. E. Chen, R. Li, N. B. Kolhe, R. Giridharagopal, S. A. Jenekhe, L. J. Richter, D. S. Ginger, *J. Am. Chem. Soc.* **2022**, *145*, 1866.
[35] T. J. Quill, G. Lecroy, D. M. Halat, R. Sheelamanthula, A. Marks, L. S. Grundy, I. Mcculloch, J. A. Reimer, N. P. Balsara, A. Giovannitti, A. Salleo, C. J. Takacs, *Nat. Mater.* **2023**, *22*, 362.
[36] C. Cheng, S. Wong, G. LeCroy, S. Schneider, E. Gomez, M. F. Toney, A. Salleo, *Adv. Energy Mater.* **2023**, *13*, 2204297.
[37] A. R. Chew, R. Ghosh, V. Pakhnyuk, J. Onorato, E. C. Davidson, R. A. Segalman, C. K. Luscombe, F. C. Spano, A. Salleo, *Adv. Funct. Mater.* **2018**, *28*, 1804142.
[38] D. A. Stanfield, Z. Mehmedovic, B. J. Schwartz, *Chem. Mater.* **2021**, *33*, 8489.
[39] J. Niklas, K. L. Mardis, B. P. Banks, G. M. Grooms, A. Sperlich, V. Dyakonov, S. Beaupré, M. Leclerc, T. Xu, L. Yu, O. G. Poluektov, *Phys. Chem. Chem. Phys.* **2013**, *15*, 9562.
[40] R. Ghosh, A. R. Chew, J. Onorato, V. Pakhnyuk, C. K. Luscombe, A. Salleo, F. C. Spano, *J. Phys. Chem. C* **2018**, *122*, 18048.
[41] P. Cavassin, I. Holzer, D. Tsokkou, O. Bardagot, J. Réhault, N. Banerji, *Adv. Mater.* **2023**, *35*, 2300308.
[42] A. L. Efros, B. I. Shklovskii, *J. Phys. C: Solid State Phys.* **1975**, *8*, L49.
[43] K. Xu, T.-P. Ruoko, M. Shokrani, D. Scheunemann, H. Abdalla, H. Sun, C.-Y. Yang, Y. Puttisong, N. B. Kolhe, J. S. M. Figueroa, J. O.

Pedersen, T. Ederth, W. M. Chen, M. Berggren, S. A. Jenekhe, D. Fazzi, M. Kemerink, S. Fabiano, *Adv. Funct. Mater.* **2022**, *32*, 2112276.

[44] D. Ofer, R. M. Crooks, M. S. Wrighton, *J. Am. Chem. Soc.* **1990**, *112*, 7869.

[45] I. E. Jacobs, G. D. ' Avino, V. Lemaur, Y. Lin, Y. Huang, C. Chen, T. Harrelson, W. Wood, L. J. Spalek, T. Mustafa, C. A. O'keefe, X. Ren, D. Simatos, D. Tjhe, M. Statz, J. W. Strzalka, J.-K. Lee, I. Mcculloch, S. Fratini, D. Beljonne, H. Sirringhaus, **2022**, *144*, 3005.

[46] K. G. Cho, D. Z. Adrahtas, K. H. Lee, C. D. Frisbie, *Adv. Funct. Mater.* **2023**, *33*, 2303700.

[47] B. D. Paulsen, C. D. Frisbie, *J. Phys. Chem. C* **2012**, *116*, 3132.

[48] M. Balooch Qarai, R. Ghosh, N. J. Hestand, F. C. Spano, *J. Phys. Chem. C* **2023**, *127*, 6414.

[49] E. C. Wu, C. Z. Salamat, O. L. Ruiz, T. Qu, A. Kim, S. H. Tolbert, B. J. Schwartz, *Adv. Funct. Mater.* **2023**, *33*, 2213652.

[50] R. A. Street, A. Salleo, M. L. Chabinyc, *Phys. Rev. B: Condens. Matter Mater. Phys* **2003**, *68*, 085316.

[51] M. B. Qarai, R. Ghosh, F. C. Spano, *J. Phys. Chem. C* **2021**, *125*, 24487.

[52] N. Siemons, D. Pearce, H. Yu, S. M. Tuladhar, G. S. LeCroy, R. Sheelamanthula, R. K. Hallani, A. Salleo, I. McCulloch, A. Giovannitti, J. M. Frost, J. Nelson, **2023**, *Proc. Natl. Acad. Sci. USA 120*, 2306272120.

[53] L. Q. Flagg, C. G. Bischak, R. J. Quezada, J. W. Onorato, C. K. Luscombe, D. S. Ginger, *ACS Mater. Lett.* **2020**, *2*, 254.

[54] L. Q. Flagg, J. W. Onorato, C. K. Luscombe, V. Bhat, C. Risko, B. Levy-Wendt, M. F. Toney, C. R. Mcneill, G. Freychet, M. Zhernenkov, R. Li, L. J. Richter, *Chem. Mater.* **2023**, *35*, 3960.

[55] D. Moia, A. Giovannitti, A. A. Szumska, I. P. Maria, E. Rezasoltani, M. Sachs, M. Schnurr, P. R. F. Barnes, I. Mcculloch, J. Nelson, *Energy Environ. Sci* **2019**, *12*, 1349.

[56] D. Khodagholy, J. Rivnay, M. Sessolo, M. Gurfinkel, P. Leleux, L. H. Jimison, E. Stavrinidou, T. Herve, S. Sanaur, R. M. Owens, G. G. Malliaras, *Nat. Commun.* **2013**, *4*, 2133.

[57] G. LeCroy, C. Cendra, T. J. Quill, M. Moser, R. Hallani, J. F. Ponder, K. Stone, S. D. Kang, A. Y.-L. Liang, Q. Thiburce, I. McCulloch, F. C. Spano, A. Giovannitti, A. Salleo, *Mater. Horiz.* **2023**, *10*, 2568.

[58] J. Ilavsky, *J. Appl. Crystallogr.* **2012**, *45*, 324.

[59] S. D. Oosterhout, V. Savikhin, J. Zhang, Y. Zhang, M. A. Burgers, S. R. Marder, G. C. Bazan, M. F. Toney, *Chem. Mater.* **2017**, *29*, 3062.

[60] G. Ashiotis, A. Deschildre, Z. Nawaz, J. P. Wright, D. Karkoulis, F. E. Picca, J. Kieffer, *J. Appl. Crystallogr.* **2015**, *48*, 510.

[61] T. G. Dane, "pygix," can be found under https://github.com/tgdane/pygix, **2017**.